

Article

Effect of Double-Quenching on the Hardness and Toughness of a Wear-Resistant Steel

Jingliang Wang ^{1,2}, Rongtao Qian ¹, Song Huang ^{1,3} and Chengjia Shang ^{1,2,3,*}

¹ Collaborative Innovation Center of Steel Technology, University of Science and Technology Beijing, Beijing 100083, China

² Yangjiang Branch, Guangdong Laboratory for Materials Science and Technology (Yangjiang Advanced Alloys Laboratory), Yangjiang 529500, China

³ State Key Laboratory of Metal Materials for Marine Equipment and Application, Anshan 114021, China

* Correspondence: cjshang@ustb.edu.cn

Abstract: Martensitic/bainitic wear-resistant steels are widely used in civilian industry, where a good combination of strength and toughness is required. In the present study, a double-quenching process was applied and compared to the conventional single-quenching process. The microhardness and ductile–brittle transition temperature were measured, and the microstructure was characterized with scanning electron microscopy and electron backscatter diffraction (EBSD) technique. It was found that the double-quenching process refined the prior austenite grain size by 43% and simultaneously improved the toughness and hardness. The ductile-to-brittle transition temperature was decreased from $-77\text{ }^{\circ}\text{C}$ to $-90\text{ }^{\circ}\text{C}$, and the hardness was increased by 8%. Based on the EBSD data, a detailed analysis of the grain boundary distribution was performed using a recently developed machine learning model. Unlike what was found in previous studies, for the studied wear-resistant steel, the refinement of the prior austenite grain did not increase the block boundary density while increasing the high-angle packet boundary density. As a result, the total density of the high-angle grain boundaries in the double-quenched specimen was not improved compared to the single-quenched specimen. Further inspection suggested that it is the prior austenite grain boundaries and high-angle packet boundaries that contribute to the hardness and toughness, and the key factors that determine their effectiveness are the high misorientation angle between the $\{110\}$ slip planes and the high slip transmission factor.



Citation: Wang, J.; Qian, R.; Huang, S.; Shang, C. Effect of Double-Quenching on the Hardness and Toughness of a Wear-Resistant Steel. *Metals* **2023**, *13*, 61. <https://doi.org/10.3390/met13010061>

Academic Editor: Andre Paulo Tschiptschin

Received: 5 December 2022

Revised: 15 December 2022

Accepted: 23 December 2022

Published: 26 December 2022



Copyright: © 2022 by the authors. Licensee MDPI, Basel, Switzerland. This article is an open access article distributed under the terms and conditions of the Creative Commons Attribution (CC BY) license (<https://creativecommons.org/licenses/by/4.0/>).

Keywords: martensitic and bainitic steels; grain boundaries; toughness; crystallography; high-strength low-alloy steels; wear-resistant steels; heat treatment

1. Introduction

Martensitic wear-resistant steels are widely employed in civil constructions, where a combination of high strength and high toughness is of great importance. While as-quenched martensite provides a sufficient hardness, a subsequent tempering process is needed to achieve the required toughness. Multiple studies have been carried out to investigate the effects of quenching and tempering conditions on the mechanical properties of wear-resistant steels. While the impact toughness can be improved by an appropriate increase in the tempering temperature, temper embrittlement takes place when the tempering temperature exceeds a critical value. Meanwhile, the hardness decreases constantly with increasing tempering temperature [1–3]. On the other hand, simultaneous improvements in strength and toughness can be achieved by grain refinement via lowering the quenching temperature. Haiko et al. altered the re-austenitization (quenching) temperatures of an as-quenched 500 HB wear-resistant steel and found that a finer prior austenite grain (PAG) size led to a significant improvement in low-temperature impact toughness and a slight increase in hardness [4]. Cyclic quenching (re-austenitizing and quenching two or more times) has also proved to be an effective way to refine the grain size and improve the

comprehensive properties of a wide range of steels [5–10]. However, so far, studies on the cyclic quenching of martensitic/bainitic wear-resistant steels are still scarce.

In the martensitic/bainitic microstructure, a PAG is divided into several packets. Each packet consists of laths with the same habit plane and is further divided into blocks consisting of laths with similar orientations [11]. Corresponding to the hierarchical microstructure, there are different types of grain boundaries. While the positive effect of grain refinement on the mechanical properties of steels is commonly described by the Hall–Petch relationship, the ‘effective’ grain size, or in other words, the effective grain boundary governing the relevant properties in a martensitic/bainitic microstructure, is still under debate. Concerning the toughness, Wang et al. proposed that packet boundaries strongly hindered fracture propagation and packets acted as the effective microstructure unit for cleavage [8]. It was also reported that the finer packet size or higher density of packet boundaries decreased the ductile-to-brittle transition temperature (DBTT) [12,13]. Zhang et al. argued that block boundaries dominate the high-angle boundaries and blocks should be the minimum structure unit controlling the toughness [14]. As reported in Ref. [15], there were many studies that supported that the block boundary is the key microstructural feature dominating the toughness and strength. Morito et al. analyzed the yield strengths of low-carbon martensitic steels with respect to the packet and block sizes, respectively, and the results suggested that the block size is the key structural parameter for the strength [16]. Wang et al. [17] also found a near-linear relationship between the block boundary density and the hardness of two bainitic/martensitic steels.

The overall misorientation angle (OMA), or simply the misorientation angle, was usually used as the criterion to define high-angle or low-angle grain boundaries. It has long been recognized that the high-angle (OMA) grain boundaries are effective in impeding crack propagation. Guo et al proposed, more specifically, that the crystallographic feature that governs transgranular fracture is the {100} cleavage plane, while the dislocation plasticity is governed by the {110} slip plane [18]. The specific misorientation angle (SMA), as opposed to the OMA, was thus proposed to describe the misorientation relationship (OR) [13,19,20]. The SMA was defined as the angle between specific crystallographic planes of two neighboring sub-volumes. The SMAs between {100} cleavage planes ({100}-SMA) and between {110} slip planes ({110}-SMA) were considered to be relevant to the cleavage fracture and dislocation gliding, respectively. In low-carbon martensitic/bainitic steels, the parent austenite phase and product phase often hold the Kurdjumov–Sachs (K–S) relationship, which is characterized by the parallelism between close-packed planes and directions in the two phases: $\{111\}_\gamma \parallel \{110\}_\alpha$ and $\langle 110 \rangle_\gamma \parallel \langle 111 \rangle_\alpha$. Due to symmetry, for the K–S relationship there are four possible habit planes, $(111)_\gamma$, $(\bar{1}\bar{1}\bar{1})_\gamma$, $(1\bar{1}\bar{1})_\gamma$, and $(\bar{1}\bar{1}1)_\gamma$, i.e., four packets within a PAG, and there are six variants, i.e., six blocks within each packet. Theoretically, there are three possible inter-variant OMAs, 10.53° , 49.47° , and 60° , within a packet [11], and in practice small deviations from the theoretical OR are usually observed. In the following, the inter-variant boundaries within a packet with an OMA smaller and greater than 15° are referred to as sub-block boundaries and block boundaries, respectively. The packet boundaries with OMA values smaller and greater than 40° are referred to as low-angle and high-angle packet boundaries, respectively. In summary, each inter-variant grain boundary within a PAG holds a theoretically fixed OR and can be categorized as a packet or block/sub-block boundary, while there are no defined ORs for PAG boundaries (PAGBs). A machine learning model was developed to distinguish different types of grain boundaries based on their features in four parameters: OMA, {100}-SMA, {110}-SMA, and {111}-SMA [13]. For example, a sub-block or block boundary must have a {110}-SMA close to zero due to the K–S relationship, while a packet boundary usually has a larger {110}-SMA.

In the present study, the effect of the double-quenching process on a wear-resistant steel was examined. The mechanical properties and microstructure of a double-quenched specimen were compared with those of a single-quenched specimen. Special attention was paid to the distribution of different types of grain boundaries, and the key microstructural

feature that affects the mechanical properties of the martensitic/bainitic wear-resistant steel is discussed.

2. Materials and Methods

The as-rolled NM400 wear-resistant steel plate was received from the industry with the chemical composition listed in Table 1. Two groups of specimens were prepared. The first group was austenitized at 900 °C and then quenched in oil; the process was repeated for the second group, as illustrated in Figure 1. These specimens are denoted as single-quenched (SQ900) and double-quenched (DQ900), respectively. After the heat treatment, the specimens were machined into 10 mm × 10 mm × 55 mm V-notched Charpy test specimens following the ASTM standard, and instrumented Charpy impact tests were performed at various temperatures ranging from −120 °C to −40 °C. Three tests were performed for each condition. Vickers hardness tests were performed on the heat-treated specimens at 1 kgf, and the microstructure was characterized with a scanning electron microscope (SEM) and electron backscatter diffraction (EBSD). A TESCAN MIRA3 SEM system equipped with an Oxford Instruments Symmetry EBSD detector was employed for the SEM and EBSD analyses. For SEM imaging, the specimens were prepared by the standard metallographic method, including grinding with silicon carbide sandpapers and polishing with diamond polishing paste, followed by etching with 4% nital. For EBSD measurements, the specimens were electropolished after the mechanical polishing using a solution with 10% perchloric acid, 5% glycerol, and 85% ethanol.

Table 1. Chemical composition of the studied steel.

Element	C	Si	Mn	Cr + Mo	Nb + Ti	B	Fe
mass%	≤0.20	≤0.30	≤1.10	0.7–0.9	≤0.04	≤0.002	Bal.

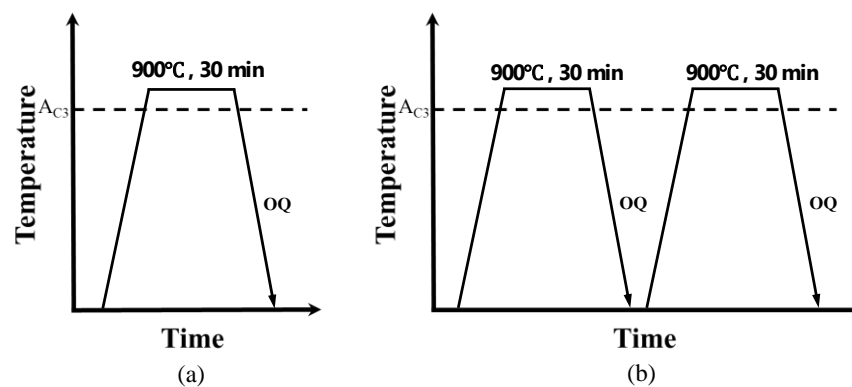


Figure 1. Heat treatment processes of single-quenched (a) and double-quenched (b) specimens.

The EBSD data were analyzed with the machine learning model, as presented in Ref. [13]. The types of the grain boundaries (PAGBs, high-angle packet boundaries, low-angle packet boundaries, block boundaries, and sub-block boundaries) were determined based on the K–S relationship using the model.

3. Results

3.1. Mechanical Properties

Figure 2a shows the total absorbed energy as a function of the temperature at which the Charpy test was performed. The DBTT was shifted from −77 °C to −90 °C by the extra quenching process, which suggests an improvement in the toughness. In contrast to the tempering process, where the increase in toughness is always associated with a degradation in hardness, the double-quenching process also led to a slight improvement in hardness: the microhardness increased from 379.7 HV to 408.5 HV (Figure 2b), with both meeting the requirement for the hardness of an NM400 steel.

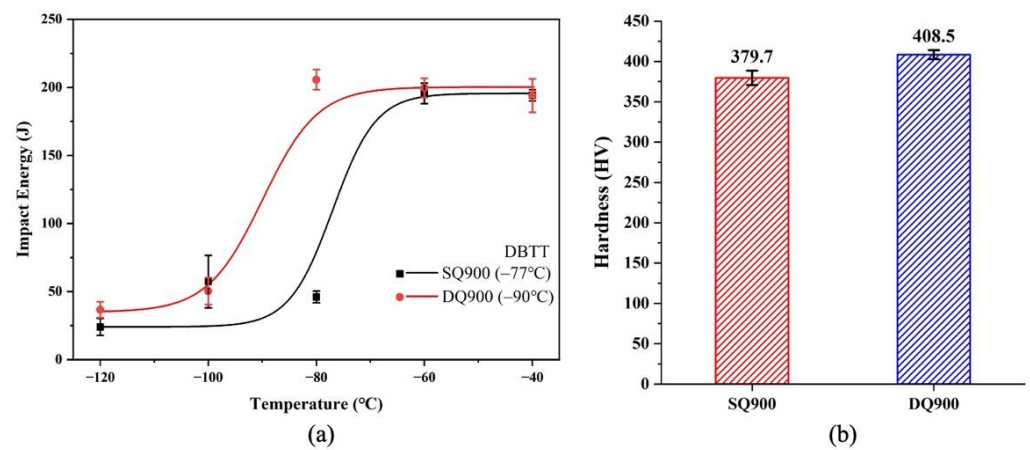


Figure 2. Impact energy–temperature curves (a) and microhardness (b) of the single-quenched and double-quenched specimens.

Unlike conventional Charpy impact tests, which only give the total absorbed energy, instrumented Charpy tests also record the impact load/energy–displacement curves. Figure 3 displays the curves measured at $-80\text{ }^{\circ}\text{C}$, which is between the DBTT of the single-quenched and double-quenched specimens. The curves can be divided into two parts: the crack initiation stage and the crack propagation stage. The cracks were initiated at the maximum load (F_m), and beyond F_m the crack propagated steadily until a critical crack length was reached. After that, unstable crack propagation took place, manifested as a sudden drop in the impact load. The absorbed energy at F_m was the crack initiation energy (CIE), as illustrated in Figure 3, and the difference between the total absorbed energy and CIE was the crack propagation energy (CPE). The CIEs for the single-quenched and double-quenched specimens were quite similar (34 J and 38 J, respectively), and it was the distinct CPEs (16 J and 176 J, respectively) that accounted for the remarkably different total impact energies (50 J and 214 J, respectively) at $-80\text{ }^{\circ}\text{C}$. It is clear that the double-quenched specimen underwent a longer ductile propagation [21] and exhibited a much better plasticity.

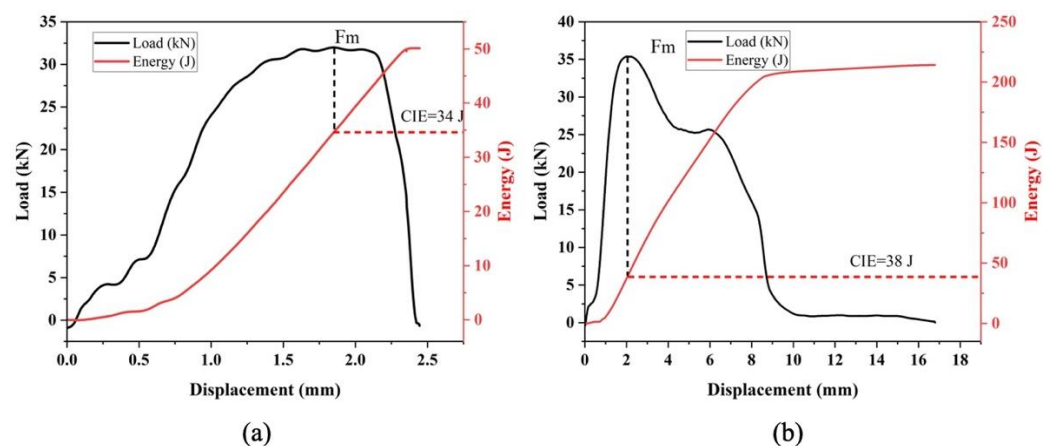


Figure 3. The impact load (energy)–displacement curves of the single-quenched (a) and double-quenched specimens (b) measured at $-80\text{ }^{\circ}\text{C}$.

3.2. Microstructure Characterization

SEM images of the heat-treated specimens are shown in Figure 4. Both single-quenched and double-quenched specimens exhibited granular bainitic microstructures with fine, dispersed martensite/austenite islands, resembling that of a water-quenched and tempered NM400 steel with a similar chemical composition [22]. The PAGBs could be visualized, as the arrows indicate. It can be seen that the double-quenched specimen had a much smaller prior austenite grain size than the single-quenched specimen. As reported in the literature, the PAG size can be effectively refined by cyclic quenching due to more nuclei for austenite reversion generated from the preceding quenching [5,7,23].

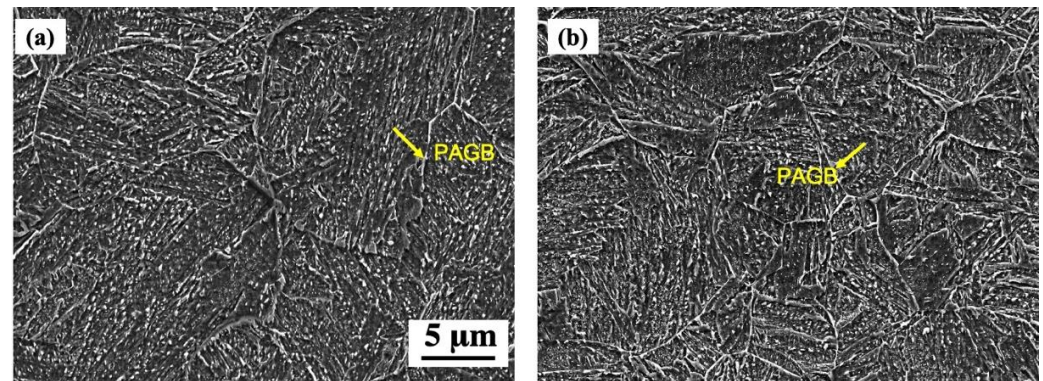


Figure 4. SEM images of the single-quenched (a) and double-quenched specimens (b).

Figure 5a presents the EBSD band contrast (BC) maps overlapped with grain boundaries shown as lines colored according to their OMAs. In Figure 5b, the grain boundaries are colored according to their types, with PAGBs shown separately in Figure 5c for the convenience of visualization. The PAG size was measured by the intercept method based on three sets of EBSD data for each specimen, and the average PAG size decreased from $12.7 \pm 2.6 \mu\text{m}$ to $7.3 \pm 0.6 \mu\text{m}$ by the double-quenching process. It can clearly be seen that the double-quenching process effectively refined and homogenized the PAG size. However, from Figure 5a,b, it seems that the total density of high-angle grain boundaries (with OMA $> 45^\circ$) was reduced by the double-quenching process, which was confirmed by the quantitative analysis shown in Figure 6: double-quenching led to a higher PAGB density, corresponding to the decreased PAG size and a higher high-angle packet boundary density. However, the double-quenched specimen showed a much smaller block boundary density compared to the single-quenched specimen. As the block boundaries accounted for the majority of the high-angle grain boundaries, the total density of the high-angle grain boundaries of the double-quenched specimens was smaller than that of the single-quenched specimen.

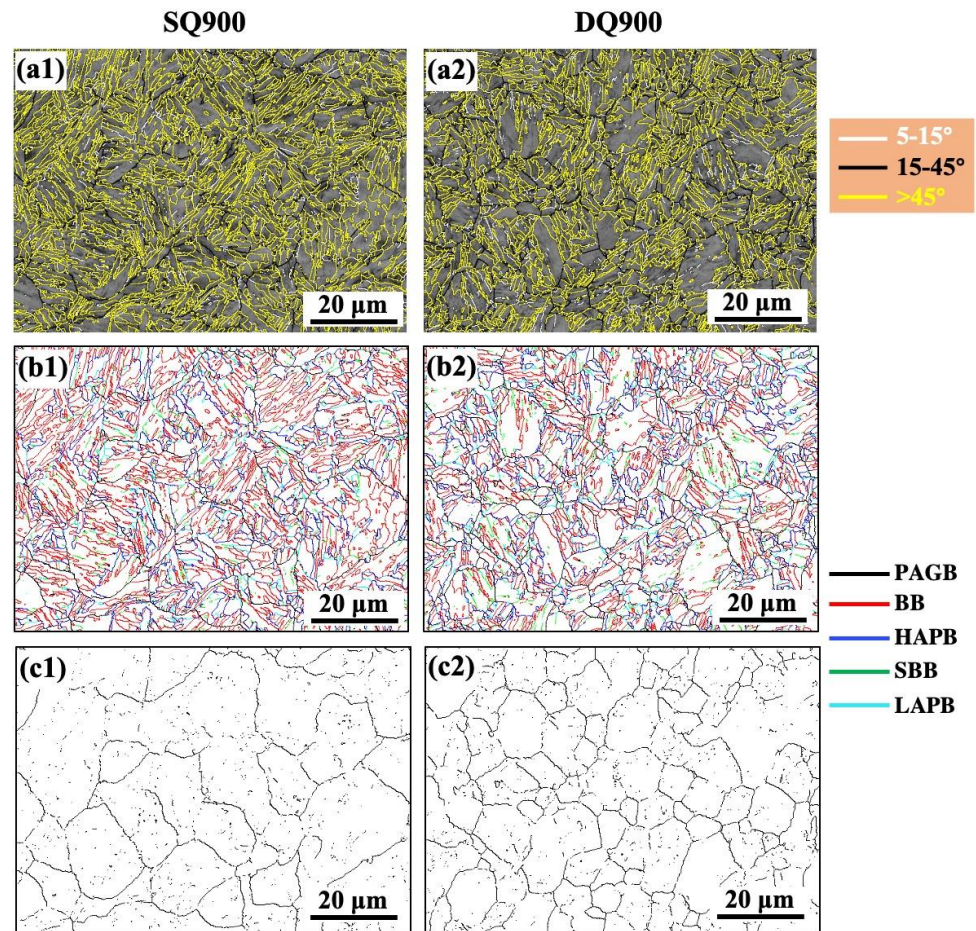


Figure 5. (a) EBSD band contrast map overlapped with grain boundaries, where lines of different colors represent different overall misorientation angles; (b) Grain boundary maps, where lines of different colors represent different types (PAGB: prior austenite grain boundary, HAPG: high-angle packet boundary, BB: block boundary, LAPG: low-angle packet boundary, SBB: sub-block boundary); (c) Prior austenite grain boundaries. The left and right columns are maps for the single-quenched and double-quenched specimens, respectively.

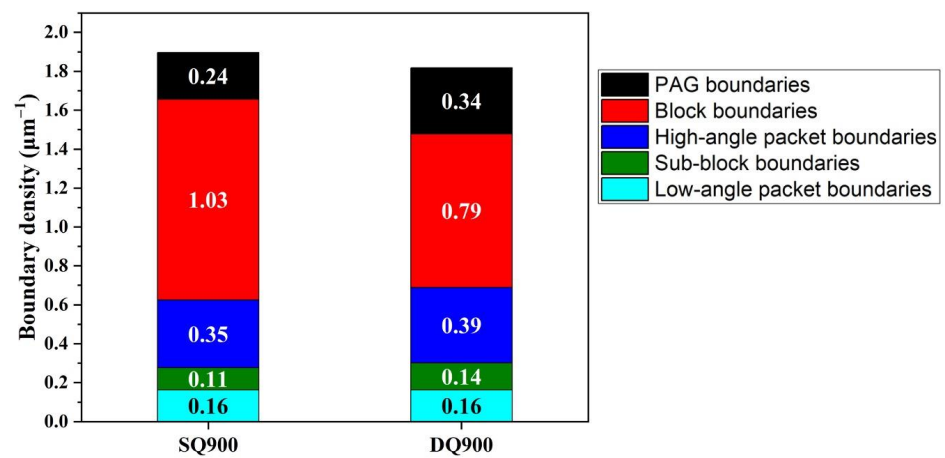


Figure 6. Density of grain boundaries of different types in the single-quenched and double-quenched specimens, quantified based on the EBSD data shown in Figure 5b.

4. Discussion

4.1. Effective Grain Boundaries for DBTT

The refinement of PAG size was reported to decrease both the packet and block sizes in lath martensite structures after quenching [5,24]. However, our results suggested that the double-quenched specimen showed a lower block boundary density compared to the single-quenched specimen. Our finding was consistent with Wang et al.'s work [25], where smaller PAGs were shown to have lower block boundary densities. The results imply that the block boundaries are not responsible for the improvement in the toughness and hardness. It is thus inferred that although both high-angle packet and block boundaries have a high OMA, their roles as barriers are quite different. The $\{110\}$ -SMA was considered to control the plastic deformation because $\{110\}$ planes are primary slip planes. Therefore, the grain boundary with a high $\{110\}$ -SMA defines the effective grain within which the free slip can occur. As seen in Figure 3, the lowering of DBTT by the double-quenching process was owing to the high plastic deformation. Therefore, we looked into the $\{110\}$ -SMA distribution in the two specimens, as shown in Figure 7a. Comparing Figure 7a to Figure 5b, we can see that the high $\{110\}$ -SMA grain boundaries are mostly PAGBs and high-angle packet boundaries, which can be seen more clearly from the quantitative analysis (Figure 7b). The $\{110\}$ -SMA of block boundaries are mostly below 5° , while those of high-angle packet boundaries are mostly between 5° and 15° . The majority of PAGBs also had $\{110\}$ -SMAs greater than 5° . As a result, although the total density of high-angle (OMA) grain boundaries in the double-quenched specimen was smaller than that of the single-quenched specimen, the total density of the high- $\{110\}$ -SMA grain boundaries was higher, as shown in Figure 8. The high density of PAGBs and high-angle packet boundaries in the double-quenched specimen would contribute effectively to the resistance to dislocation gliding. The high plastic deformation of the double-quenched specimen thus seems counterintuitive. However, it was also reported in other works that the refinement of PAG and packet size decreased the DBTT [12,13], consistent with our finding. A plausible explanation is that the fine effective grains for slip decentralized the stress concentration at the crack tip, so the unstable crack propagation was delayed. This was confirmed in Figure 3, where one can see a prolonged crack propagation stage for the double-quenched specimen.

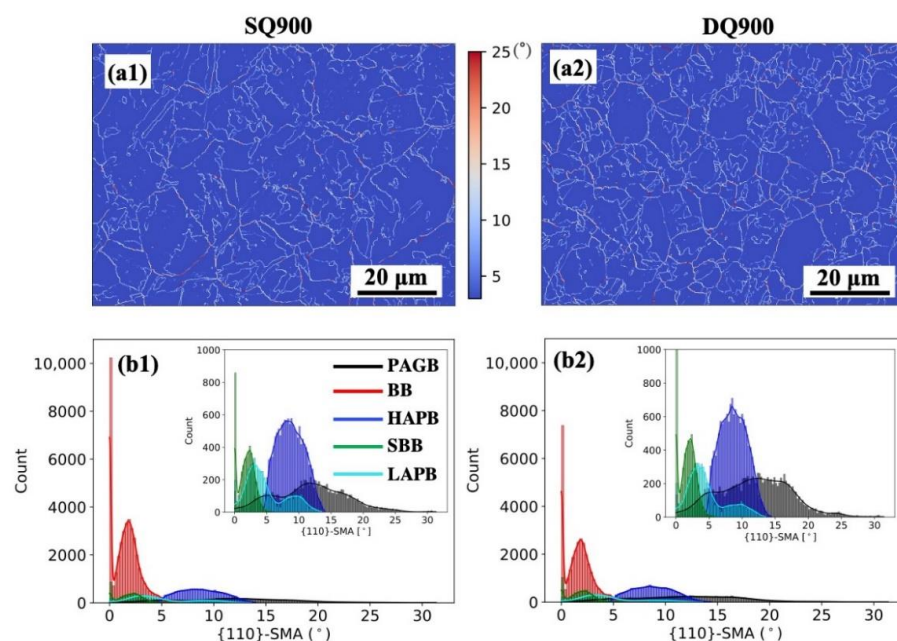


Figure 7. A $\{110\}$ -SMA distribution map (a) and $\{110\}$ -SMAs of different types of grain boundaries (b) of single-quenched (left column) and double-quenched (right column) specimens (PAGB: prior austenite grain boundary, HAPG: high-angle packet boundary, BB: block boundary, LAPG: low-angle packet boundary, SBB: sub-block boundary).

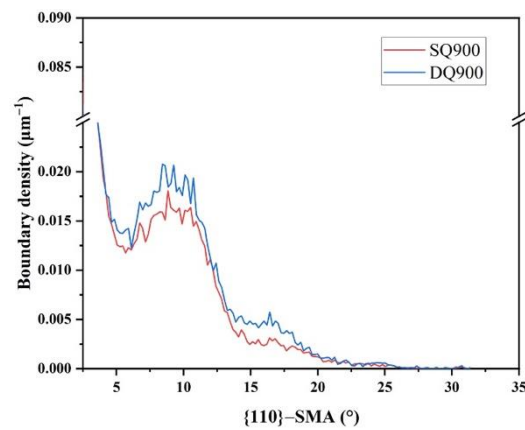


Figure 8. Density of boundaries with different {110}-SMAs.

4.2. Effective Grain Boundaries for Hardness

In previous studies, block boundaries were considered to be most relevant to the hardness [17]. In the present study, however, the double-quenched specimen with a lower block boundary density had a slightly higher hardness. The hardness reflects the resistance against localized plastic deformation, i.e., dislocation movement [26]. Therefore, the concept of {110}-SMA seems to also work for the hardness. In that sense, PAGBs and high-angle packet boundaries also contributed to the hardness.

Apart from {110}-SMA, we also calculated the slip transmission factor m' , which was defined as $m' = \cos(\varphi)\cos(\kappa)$, where φ is the angle between the slip directions in neighboring crystallographic units ('grains') and κ is the angle between normal to the slip planes of neighboring grains. The slip transmission factor is thus a geometric factor to measure the ability of slip transfer between neighboring grains without losing the coherency at the grain boundary [27]. The slip transmission factor between different variants was reported to be closely related to the plasticity and strength/hardness [28,29]. By definition, the higher the m' , the more transparent a grain boundary for a specific slip system. In this study, we took the N value, the maximum m' of all slip systems in the adjacent sub-volumes, to indicate the ease of slip transmission of a grain boundary. In other words, the grain boundary with a larger 1-N value is more resistant to slip transmission. The distribution maps of 1-N values are shown in Figure 9a, and the quantitative results are plotted in Figure 9b. In contrast to the {110}-SMA, the 1-N value of the high-angle packet boundary shows a bimodal distribution, while it is still the PAGB and high-angle packet boundary that contribute most to the high 1-N values. Therefore, the double-quenched specimen also showed a higher 1-N value than the single-quenched specimen (Figure 10), i.e., a higher resistance to plastic deformation and hence higher hardness.

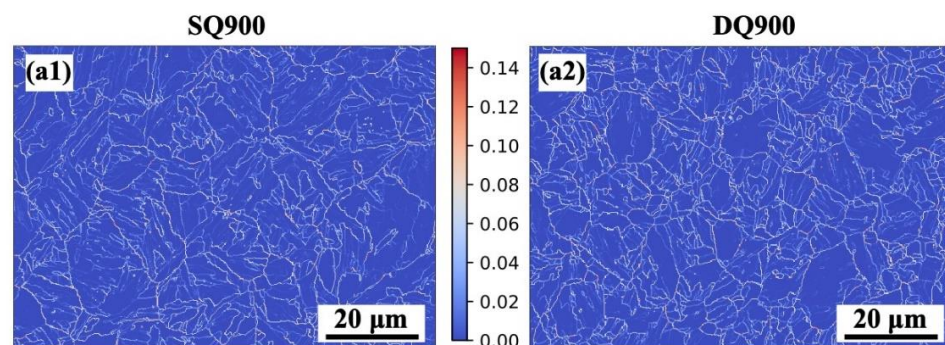


Figure 9. Cont.

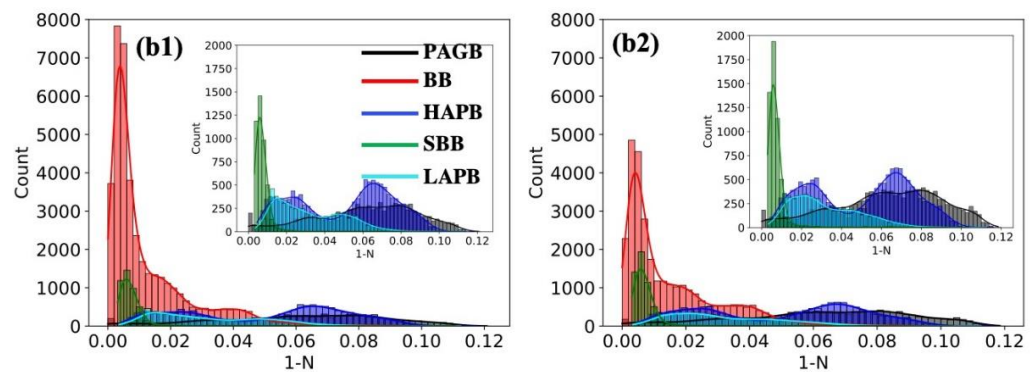


Figure 9. The 1-N value distribution map (a) and 1-N values of different types of grain boundaries (b) of single-quenched (left column) and double-quenched (right column) specimens (PAGB: prior austenite grain boundary, HAPG: high-angle packet boundary, BB: block boundary, LAPG: low-angle packet boundary, SBB: sub-block boundary).

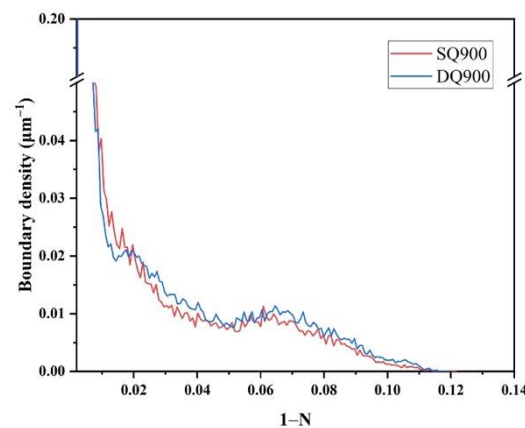


Figure 10. Density of boundaries with different 1-N values.

5. Conclusions

Compared to the conventional single-quenching process, the application of double-quenching to the wear-resistant steel refined the PAG size significantly and improved both the hardness and impact toughness. The quantitative analysis of the grain boundaries indicated that the double-quenched specimen had a higher PAGB and high-angle packet boundary density, while it showed a lower block boundary density. Further inspection suggested that both the PAGB and high-angle packet boundary showed high $\{110\}$ -SMA and 1-N values compared to the other types of grain boundaries. Therefore, they were more effective in hindering dislocation movement, which reduced the stress concentration at the crack tip during the Charpy test. Meanwhile, the restriction of dislocation movement also contributed positively to the hardness.

Author Contributions: Conceptualization, C.S.; methodology, C.S. and J.W.; formal analysis, J.W. and R.Q.; investigation, R.Q. and S.H.; resources, S.H., J.W. and C.S.; data curation, J.W. and R.Q.; writing—original draft preparation, J.W.; writing—review and editing, J.W.; visualization, R.Q. and J.W.; supervision, J.W. and C.S.; funding acquisition, C.S. and J.W. All authors have read and agreed to the published version of the manuscript.

Funding: This research was funded by the National Natural Science Foundation of China (grant number 52271089) and the Fundamental Research Funds for the Central Universities (grant number FRF-IC-20-04).

Data Availability Statement: The data presented in this study are available on request from the corresponding author.

Acknowledgments: The authors are grateful to Jingxiao Zhao for his help with the grain boundary analysis.

Conflicts of Interest: The authors declare no conflict of interest.

References

1. Wen, E.; Song, R.; Xiong, W. Effect of tempering temperature on microstructures and wear behavior of a 500 HB grade wear-resistant steel. *Metals* **2019**, *9*, 45. [[CrossRef](#)]
2. Cao, Y.; Wang, Z.; Kang, J.; Wu, D.; Wang, G. Effects of tempering temperature and Mo/Ni on microstructures and properties of lath martensitic wear-resistant steels. *J. Iron Steel Res. Int.* **2013**, *20*, 70–75. [[CrossRef](#)]
3. Fu, H.; Xiao, Q.; Fu, H. Heat treatment of multi-element low alloy wear-resistant steel. *Mater. Sci. Eng. A* **2005**, *396*, 206–212. [[CrossRef](#)]
4. Haiko, O.; Javaheri, V.; Valtonen, K.; Kaijalainen, A.; Hannula, J.; Kömi, J. Effect of prior austenite grain size on the abrasive wear resistance of ultra-high strength martensitic steels. *Wear* **2020**, *454*, 203336. [[CrossRef](#)]
5. Furuhashi, T.; Kikumoto, K.; Saito, H.; Sekine, T.; Ogawa, T.; Morito, S.; Maki, T. Phase transformation from fine-grained austenite. *ISIJ Int.* **2008**, *48*, 1038–1045. [[CrossRef](#)]
6. Kamada, Y.; Ohnishi, K.; Bessyo, K. Effect of double-quench processing on toughness of heavy-gauge ultrahigh strength steel plate. *J. Mater. Sci. Lett.* **1991**, *10*, 598–601. [[CrossRef](#)]
7. Lee, K.; Hong, S.; Kang, Y.; Yoon, H.; Kang, S. Grain refinement in bearing steels using a double-quenching heat-treatment process. *Int. J. Automot. Technol.* **2009**, *10*, 697–702. [[CrossRef](#)]
8. Wang, C.; Wang, M.; Shi, J.; Hui, W.; Dong, H. Effect of microstructural refinement on the toughness of low carbon martensitic steel. *Scripta Mater.* **2008**, *58*, 492–495. [[CrossRef](#)]
9. Sanij, M.K.; Banadkouki, S.G.; Mashreghi, A.; Moshrefifar, M. The effect of single and double quenching and tempering heat treatments on the microstructure and mechanical properties of AISI 4140 steel. *Mater. Des.* **2012**, *42*, 339–346. [[CrossRef](#)]
10. Cao, Z.; Shi, Z.; Yu, F.; Sugimoto, K.-i.; Cao, W.; Weng, Y. Effects of double quenching on fatigue properties of high carbon bearing steel with extra-high purity. *Int. J. Fatigue* **2019**, *128*, 105176. [[CrossRef](#)]
11. Morito, S.; Tanaka, H.; Konishi, R.; Furuhashi, T.; Maki, T. The morphology and crystallography of lath martensite in Fe-C alloys. *Acta Mater.* **2003**, *51*, 1789–1799. [[CrossRef](#)]
12. Liu, D.; Luo, M.; Cheng, B.; Cao, R.; Chen, J. Microstructural evolution and ductile-to-brittle transition in a low-carbon MnCrMoNiCu heavy plate steel. *Metall. Mater. Trans. A* **2018**, *49*, 4918–4936. [[CrossRef](#)]
13. Li, X.; Zhao, J.; Cong, J.; Misra, R.; Wang, X.; Wang, X.; Shang, C. Machine learning guided automatic recognition of crystal boundaries in bainitic/martensitic alloy and relationship between boundary types and ductile-to-brittle transition behavior. *J. Mater. Sci. Technol.* **2021**, *84*, 49–58. [[CrossRef](#)]
14. Zhang, C.; Wang, Q.; Ren, J.; Li, R.; Wang, M.; Zhang, F.; Sun, K. Effect of martensitic morphology on mechanical properties of an as-quenched and tempered 25CrMo48V steel. *Mater. Sci. Eng. A* **2012**, *534*, 339–346. [[CrossRef](#)]
15. Morris Jr, J.W. Comments on the microstructure and properties of ultrafine grained steel. *ISIJ Int.* **2008**, *48*, 1063–1070. [[CrossRef](#)]
16. Morito, S.; Yoshida, H.; Maki, T.; Huang, X. Effect of block size on the strength of lath martensite in low carbon steels. *Mater. Sci. Eng. A* **2006**, *438*, 237–240. [[CrossRef](#)]
17. Wang, J.; Hong, H.; Huang, A.; Yang, X.; Qian, R.; Shang, C. New insight into the relationship between grain boundaries and hardness in bainitic/martensitic steels from the crystallographic perspective. *Mater. Lett.* **2022**, *308*, 131105. [[CrossRef](#)]
18. Guo, Z.; Lee, C.; Morris Jr, J. On coherent transformations in steel. *Acta Mater.* **2004**, *52*, 5511–5518. [[CrossRef](#)]
19. Zhao, J.; Li, X.; Wang, X.; Liu, S.; Wang, X.; Shang, C. Distribution feature of specific misorientation angle in a bainitic steel. *Mater. Charact.* **2021**, *172*, 110874. [[CrossRef](#)]
20. Li, X.; Zhao, J.; Wang, J.; Wang, X.; Liu, S.; Shang, C. Effect of boundaries on toughness in high-strength low-alloy steels from the view of crystallographic misorientation. *Mater. Lett.* **2020**, *259*, 126841. [[CrossRef](#)]
21. Song, H.; Li, C.; Lan, L.; Zhao, D.; Wang, G. Impact toughness of an NM400 wear-resistant steel. *J. Iron Steel Res. Int.* **2013**, *20*, 72–77. [[CrossRef](#)]
22. Huang, S.; Yu, Y.; Wang, Z.; Su, S.; Chen, K.; Yuan, S.; Xie, Z.; Shang, C. Crystallographic insights into the role of nickel on hardenability of wear-resistant steels. *Mater. Lett.* **2022**, *306*, 130961. [[CrossRef](#)]
23. Yuan, S.; Xie, Z.; Wang, J.; Zhu, L.; Yan, L.; Shang, C.; Misra, R. Effect of heterogeneous microstructure on refining austenite grain size in low alloy heavy-gage plate. *Metals* **2020**, *10*, 132. [[CrossRef](#)]
24. Li, X.; Lu, G.; Wang, Q.; Zhao, J.; Xie, Z.; Misra, R.D.K.; Shang, C. The Effects of Prior Austenite Grain Refinement on Strength and Toughness of High-Strength Low-Alloy Steel. *Metals* **2021**, *12*, 28. [[CrossRef](#)]
25. Wang, X.; Wang, Z.; Ma, X.; Subramanian, S.; Xie, Z.; Shang, C.; Li, X. Analysis of impact toughness scatter in simulated coarse-grained HAZ of E550 grade offshore engineering steel from the aspect of crystallographic structure. *Mater. Charact.* **2018**, *140*, 312–319. [[CrossRef](#)]
26. Hugosson, H.W.; Jansson, U.; Johansson, B.; Eriksson, O. Restricting dislocation movement in transition metal carbides by phase stability tuning. *Science* **2001**, *293*, 2434–2437. [[CrossRef](#)]

27. Weaver, J.S.; Li, N.; Mara, N.A.; Jones, D.R.; Cho, H.; Bronkhorst, C.A.; Fensin, S.J.; Gray III, G.T. Slip transmission of high angle grain boundaries in body-centered cubic metals: Micropillar compression of pure Ta single and bi-crystals. *Acta Mater.* **2018**, *156*, 356–368. [[CrossRef](#)]
28. Wang, Z.; Guo, Z.; Shang, C.; Chen, B.; Hui, Y. Characterization of the Stretch Flangeability of High-Strength Bainitic Steel: The Significance of Variant Pairs. *Materials* **2021**, *15*, 276. [[CrossRef](#)]
29. Wang, Z. Study on the Correlation between Crystallography and Mechanical Properties of High Strength Steels. Ph.D. Thesis, University of Science and Technology Beijing, Beijing, China, 2022.

Disclaimer/Publisher's Note: The statements, opinions and data contained in all publications are solely those of the individual author(s) and contributor(s) and not of MDPI and/or the editor(s). MDPI and/or the editor(s) disclaim responsibility for any injury to people or property resulting from any ideas, methods, instructions or products referred to in the content.